Microscopic Engine Powered by Critical Demixing

Supplementary Information

Falko Schmidt,[1,2,3] Alessandro Magazzù,[1,2] Agnese Callegari,[2]

Luca Biancofiore,[4] Frank Cichos,[3] and Giovanni Volpe[1,2,*]

[1]*Department of Physics, University of Gothenburg, 41296 Gothenburg, Sweden*

[2]*Soft Matter Lab, Department of Physics and*

UNAM – National Nanotechnology Research Center,

Bilkent University, Ankara 06800, Turkey

[3]*Peter-Debye-Institute for Soft Matter Physics,*

Faculty of Physics and Earth Science,

University of Leipzig, 04103 Leipzig, Germany

[4]*Department of Mechanical Engineering,*

Bilkent University, Ankara 06800, Turkey

[*] giovanni.volpe@physics.gu.se

I. ABSORBING PARTICLES

The particles used in our experiments are magnetic silica particles (radius $R = 1.24 \pm 0.04\,\mu\text{m}$, produced by Microparticles GmbH). These particles are made of porous silica into which iron oxide nanoparticles are let to diffuse, and they are coated with an external layer of silica. A typical SEM image of such a particle can be seen in supplementary Fig. S1. During production, clusters of iron oxide occur at the surface changing the particle's absorption properties locally. Every single particle possesses a unique distribution of iron oxide, which is typically asymmetric and gives rise to the asymmetric diffusiophoretic drift responsible for the particle's orbital motion.

II. SETUP

The schematic of the setup is shown in supplementary Fig. S2. The optical tweezers is built on a homemade inverted microscope. The trapping laser beam ($\lambda = 976\,\text{nm}$) is focused through an oil-immersion objective ($100\times$, NA = 1.30).

The sample chamber is prepared using a microscopic slide with a cavity (liquid volume $V = 30\,\mu\text{l}$) and sealed using a coverslip. The whole sample is temperature-stabilized using a copper-plate heat exchanger coupled to a water circulating bath (T100, Grant Instruments) with $\pm 50\,\text{mK}$ temperature stability. Two Peltier elements (TEC3-6, Thorlabs) placed on the trapping objective permit us to fine-tune ($\pm 3\,\text{mK}$) the temperature using a feedback controller (TED4015, Thorlabs).

A second laser ($\lambda = 532\,\text{nm}$) is used to illuminate the sample through a $20\times$ objective (NA = 0.45) and excites the fluorescent dye Rhodamine B (C.I. 45170, Merck) dissolved in the solution. The emission peak of this dye is at $\lambda \approx 600\,\text{nm}$. A CMOS camera (DCC1645C, Thorlabs) records the light emitted by the sample at a frame rate of 296 fps. We have verified that the addition of Rhodamine B does not alter the critical properties of the solution.

The recorded videos are analyzed using standard digital video microscopy algorithms to obtain the three-dimensional position of the particle. We have found that the particle predominantly moves in the xy-plane. We have therefore neglected the information about the z-position in our analysis.

III. DIFFUSIOPHORESIS

Diffusiophoresis is the self-propulsion of particles along a concentration gradient. In our case, this concentration gradient is triggered by a local increase in temperature ΔT that leads to a local demixing of the binary solution and hence to a concentration gradient $\Delta \phi$ (as depicted in Fig. S3). The boundary between mixed and demixed regions experiences a nonuniform pressure as well as a steady current flow, which results into a slip velocity $\mathbf{v}_{\mathrm{s}}(\mathbf{r}) \propto \Delta \phi$. Depending on the particle's wetting properties (hydrophilic or hydrophobic) the sign of the resulting net motion of the particle changes (more details can be found in Ref. [1]). This behavior can be in principle scaled down to the nanoscale as long as $\mathbf{v}_{\mathrm{s}}(\mathbf{r}) \propto R^{-1}$.

IV. AMBIENT TEMPERATURE DEPENDENCE OF CRITICAL ENGINE OPERATION

We fix the laser power at $P = 2.7 \, \mathrm{mW}$ and study the behavior of the critical engine as a function of the ambient temperature T_0.

At $T_0 = 20°\mathrm{C}$, the system behaves as a standard optical trap: the particle trajectory lingers near the center of the optical trap (solid line in Suppl. Fig. S4a); the drift field points towards the optical trap center (white arrows in Suppl. Fig. S4b); $\mathcal{D}_{xy}$ is negligible (Suppl. Fig. S4c); and $\Omega \approx 0 \, \mathrm{rpm}$.

As T_0 is increased to $24°\mathrm{C}$, the particle explores a larger area around the center of the optical trap (Suppl. Fig. S4d) and rotational forces start emerging as shown by the drift field (Suppl. Fig. S4e) and by $\mathcal{D}_{xy}$ (Suppl. Fig. S4f). The corresponding average rotation of the particle is $\Omega_{xy} = 1060 \, \mathrm{rpm}$. The diffusiophoretic drift generated by the particle is however not large enough to set the particle into constant rotation around the optical axis, as can be seen from the fact that the particle trajectory occasionally crosses the center of the trap (solid line in Suppl. Fig. S4d).

At $T_0 = 26°\mathrm{C}$, the particle steadily rotates around the optical trap center (Suppl. Fig. S4g), leading to a well-defined rotational drift field (Suppl. Fig. S4h) and to an increase of $\mathcal{D}_{xy}$ (Suppl. Fig. S4i). The corresponding rotation rate is $\Omega_{xy} = 1160 \, \mathrm{rpm}$.

At even higher temperatures (i.e. $T_0 = 27°\mathrm{C}$ and $T_0 = 28°\mathrm{C}$), the particle starts to

occasionally change its orientation passing through the optical trap center before returning to its revolutionary motion (Suppl. Figs. S4j,m). With increasing T_0, the drift field looses the rotational component (Suppl. Figs. S4k,n) and $\mathcal{D}_{xy}$ decreases (Suppl. Figs. S4l,o), which are clear signatures of decreasing rotational forces. The corresponding average rotation rates are significantly affected by the frequent changes of direction leading to $\Omega_{xy} \approx 0\,\mathrm{rpm}$.

A further increase in temperature leads to the particle being pushed away from the optical trap by the presence of overwhelming diffusiophoretic drifts.

V.   PARTICLE SIZE DEPENDENCE OF CRITICAL ENGINE OPERATION

We have also demonstrated experimentally that the critical engine works for particles of different sizes. In particular, we reproduced the critical engine operation as function of laser power and ambient temperature using a smaller particle of radius $R = 0.49 \pm 0.03\,\mu\mathrm{m}$.

In Fig. S6, the engine performance is studied for a particle of radius $R = 0.49\,\mu\mathrm{m}$ at a fixed ambient temperature of $T_0 = 21°\mathrm{C}$ as a function of the laser power P (compare with Fig. 2 for $R = 1.24\,\mu\mathrm{m}$). When $P = 0.6\,\mathrm{mW}$, the particle is just optically trapped (Fig. S6a-c), and its rotation rate is $\Omega_{xy} = 0\,\mathrm{rpm}$. When the power is increased to $P = 1.5\,\mathrm{mW}$, the particle performs rotations around the trapping laser beam (Fig. S6d-f) with a rotation rate $\Omega_{xy} = 4020\,\mathrm{rpm}$. At even higher power ($P = 2.7\,\mathrm{mW}$), the particle is randomly passing through the center of the laser beam (Fig. S6g-i), leading to a decrease of its rotation rate ($\Omega_{xy} = 2860\,\mathrm{rpm}$).

In Fig. S7, the engine performance is studied for a particle of radius $R = 0.49\,\mu\mathrm{m}$ at fixed power $P = 1.5\,\mathrm{mW}$ as a function of the ambient temperature T_0 (compare with Fig. S4 for $R = 1.24\,\mu\mathrm{m}$). At $T_0 = 19.5°\mathrm{C}$, the particle is just optically trapped and features a small rotation with $\Omega_{xy} = 1200\,\mathrm{rpm}$ (Fig. S7a-c). At $T_0 = 23°\mathrm{C}$ (Fig. S6d-f), it performs continuous rotations at similar rates as in Fig. S5f ($\Omega_{xy} = 4600\,\mathrm{rpm}$). At an even higher temperature ($T_0 = 27°\mathrm{C}$), the particle stops rotating due to larger demixing on the particles surface and its motion outside the optical trap becomes completely uncorrelated (Fig. S6g-i).

Comparing the behavior of the particles with $R = 0.49\,\mu\mathrm{m}$ (Figs. S6 and S7) and $R = 1.24\,\mu\mathrm{m}$ (Figs. 2 and S4), the smaller particle reaches a higher rotation rate of $4600\,\mathrm{rpm}$, but its differential cross correlation function decays faster, since for smaller particles thermal fluctuations become more dominant. Moving towards the nanoscale, for even smaller

particles we expect the smooth rotational behavior of the critical engine to be disrupted by the increase of translational and rotational Brownian diffusion.

VI. DATA ANALYSIS

Each trajectory is analyzed by calculating the corresponding drift field, differential cross-correlation function $\mathcal{D}_{xy}$, rotation rate Ω_{xy}, and work W.

The velocity drift fields are derived from the measured trajectory as

$$\mathbf{v}(\mathbf{r}) = \frac{1}{\Delta t} \langle \mathbf{r}_{n+1} - \mathbf{r}_n | \mathbf{r}_n \approx \mathbf{r} \rangle, \tag{1}$$

where $\mathbf{r}_n$ is the position of the particle in the xy-plane and Δt is the time interval between subsequent positions of the particle. The calculated magnitude and direction of the local velocity is indicated by white arrows in Figs. 2, S4, S6 and S7.

The differential cross-correlation function $\mathcal{D}_{xy}(\tau)$ of the particle motion is calculated as [2, 3]:

$$\mathcal{D}_{xy}(\tau) = C_{xy}(\tau) - C_{yx}(\tau), \tag{2}$$

where $C_{xy}(\tau) = \frac{\langle x(t)\ y(t+\tau) \rangle}{\sqrt{\langle x(t)^2 \rangle \langle y(t)^2 \rangle}}$ and $C_{yx}(\tau) = \frac{\langle y(t)\ x(t+\tau) \rangle}{\sqrt{\langle x(t)^2 \rangle \langle y(t)^2 \rangle}}$. The theoretical expression of $\mathcal{D}_{xy}(\tau)$ for a trapped spherical particle rotating in a plane can be obtained from the Langevin equation in a non-homogeneous force field [3] as

$$\mathcal{D}_{xy}(\tau) = 2D \, \frac{e^{-\omega_\rho |\tau|}}{\omega_\rho} \sin\left(\Omega_{xy}\tau\right), \tag{3}$$

where D is the diffusion coefficient, ω_ρ is the radial relaxation frequency of the particle in the optical trap (obtained from the autocorrelation function [4]), and Ω_{xy} is the rotational frequency of the particle in the xy-plane. The value of Ω_{xy} is obtained by fitting the experimental $\mathcal{D}_{xy}(\tau)$ (Eq. (2)) to the theoretical expression in Eq. (3). The resulting hydrodynamic viscous torque is then:

$$\overline{\mathbf{\Gamma}}_{xy} = \overline{\mathbf{r} \times \mathbf{F}_{\text{drag}}} = \gamma \overline{\mathbf{r} \times \mathbf{r} \times \Omega_{xy}} = \gamma \, \Omega_{xy} \, \sigma_{xy}^2 \, \hat{\mathbf{z}}, \tag{4}$$

where $\mathbf{r}$ is the position of the particle, $\gamma = 6\pi\eta R$ is the friction coefficient, defined by Stokes law and related to the medium viscosity η and to the particle's radius R, and σ_{xy}^2 is the variance of the particle's position in the plane orthogonal to the torque.

The work performed during a single rotation about the z-axis can be expressed as [5]:

$$W = \int_0^{2\pi} \overline{\Gamma}_{xy} \, d\theta = 2\pi \, \frac{\Omega_{xy}}{\omega_\rho} \, k_{\mathrm{B}}T. \tag{5}$$

VII.   NUMERICAL SIMULATIONS

The motion of the particle is simulated using a standard finite-difference algorithm based on a three-dimensional Langevin equation describing the motion of the particle under the action of Brownian motion, optical forces, and diffusiophoretic drifts and torques [4]. The particle is modeled as a silica microsphere (radius $R = 1.24$ μm) with iron-oxide inclusions (25% of total weight) distributed inhomogeneously near the surface of the particle. The optical force on the particle is calculated using generalized Mie theory (particle refractive index $n_{\mathrm{p}} = 1.46$, medium refractive index $n_{\mathrm{m}} = 1.38$ [6]) and assuming a linearly polarized Gaussian beam (wavelength $\lambda_0 = 976$ nm) focused through a high-NA objective (NA = 1.30) [4]. The temperature increase as a function of position, $\Delta T(\mathbf{r})$, is obtained using Fourier's law of heat conduction [7]:

$$\nabla^2(\Delta T(\mathbf{r})) = -\frac{\alpha}{C}I(\mathbf{r}), \tag{6}$$

where $I(\mathbf{r})$ is the light intensity, α is the absorption coefficient of iron (for iron $\alpha = 2.43 \cdot 10^7\,\mathrm{m}^{-1}$, we assume no absorption in silica and water–2,6-lutidine), and C is the thermal conductivity (for iron $C = 73\,\mathrm{Wm}^{-1}\mathrm{K}^{-1}$, for silica $C = 1.4\,\mathrm{Wm}^{-1}\mathrm{K}^{-1}$, for water–2,6-lutidine $C = 0.39\,\mathrm{Wm}^{-1}\mathrm{K}^{-1}$). Where $T_0 + \Delta T(\mathbf{r}) > T_{\mathrm{c}}$, a concentration gradient $\Delta\phi(\mathbf{r})$ is induced, which, in proximity of the critical temperature T_{c}, is [1]

$$\Delta\phi(\mathbf{r}) = \sqrt{\frac{T_0 + \Delta T(\mathbf{r}) - T_{\mathrm{c}}}{K}}, \tag{7}$$

where K is a constant. The concentration gradient $\Delta\phi(\mathbf{r})$ generates a slip velocity field $\mathbf{v}_{\mathrm{s}}(\mathbf{r})$ in the layer around the particle. The diffusiophoretic drift is then $\mathbf{v}_{\mathrm{p}} = -\langle\mathbf{v}_{\mathrm{s}}(\mathbf{r})\rangle$ [1], while the diffusiophoretic torque is $\mathbf{T}_{\mathrm{ph}} = \langle\mathbf{r}_{\mathrm{s}} \times (-\gamma\mathbf{v}_{\mathrm{s}})\rangle$, where $\mathbf{r}_{\mathrm{s}}$ is the vector connecting the center of mass of the particle to the particle's surface. We remark that Ref. [8] suggests that at a high velocity of the particle ($> 10\,\mu\mathrm{m\,s}^{-1}$) the effect of advection around the particle plays a significant role and alters the motion of the particle compared to the model in Ref. [1]; nevertheless we have found quantitative agreement between our simulations based on Ref. [1] without advection and our experiments, suggesting that advection can be neglected in this case.

A. Supplementary Video 1

Engine performance as a function of laser power. Recorded brightfield images of the particle at a frame rate of $296\,\mathrm{Hz}$. The ambient temperature of the sample is fixed at $T_0 = 26°\mathrm{C}$, while the laser power at the optical trap is increased stepwise. See also Fig. 2.

B. Supplementary Video 2

Engine performance as a function of ambient temperature. Recorded brightfield images of the particle at a frame rate of $296\,\mathrm{Hz}$. The laser power at the optical trap is fixed at $P = 2.7\,\mathrm{mW}$, while the ambient temperature of the sample is increased stepwise. See also supplementary Fig. S4.

C. Supplementary Video 3

Simulation of a critical engine. (left) An absorbing particle in a critical mixture rotating around the center of an optical trap, (middle) corresponding temperature profiles (the isotemperature lines are spaced by $5\,\mathrm{K}$), and (right) concentrations profiles (the iso-concentration lines are spaced by 0.04) in the xy-plane ($z = 0$). See also supplementary Fig. S3.
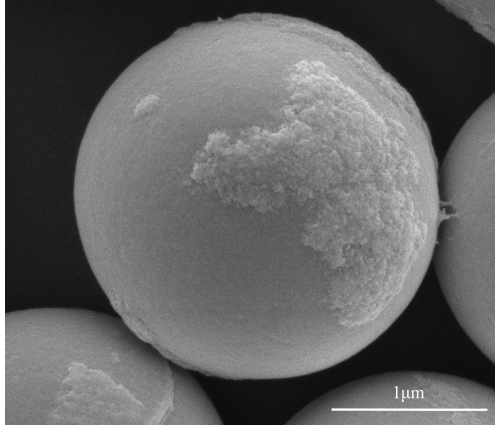
FIG. S1: Image of an absorbing microsphere acquired by scanning electron microscopy (SEM). The particle is a silica microsphere with radius $R = 1.24 \pm 0.04\,\mu$m and iron oxide inclusions. The rough regions on the surface of the microsphere correspond to iron oxide clusters.

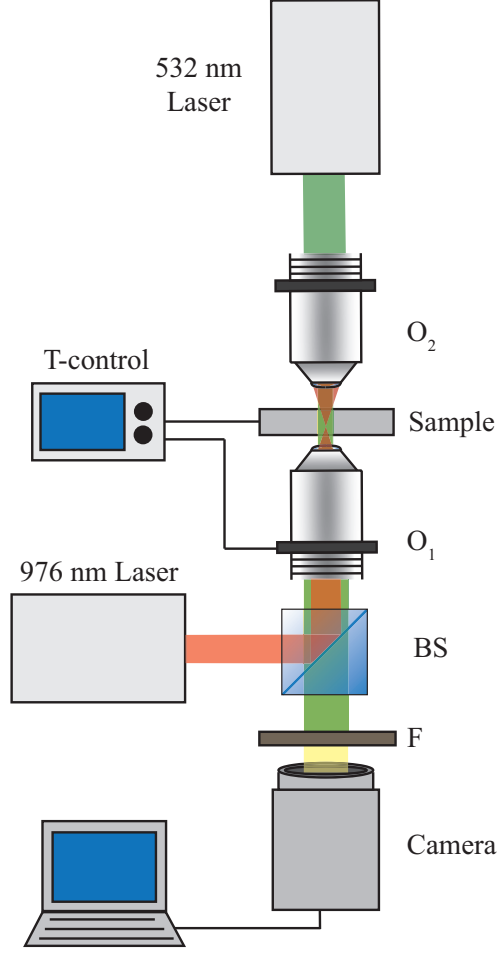FIG. S2: Schematic of the experimental setup. The trapping laser ($\lambda = 976\,\mathrm{nm}$) is reflected by the dichroic beam splitter (BS) onto objective O_1 ($100\times$, NA $= 1.30$), which focuses the light inside the temperature-stabilized sample. The whole sample is illuminated by a defocused green laser through objective O_2 ($20\times$, NA $= 0.45$); the forward-scattered light is filtered (filter F) to eliminate the excitation laser light and projected onto a camera.
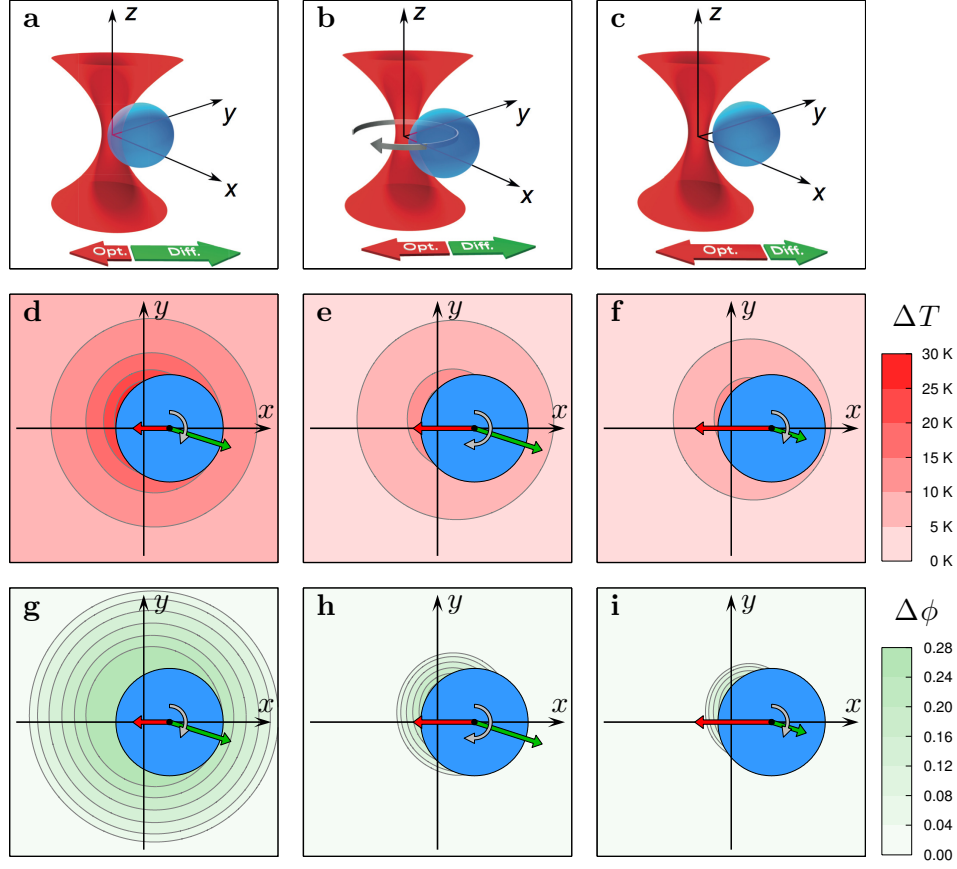
FIG. S3: Simulation of a critical engine. (a-c) Absorbing particle in a critical mixture held at various radial distances from the center of an optical trap, and corresponding (d-f) temperature profiles (the isotemperature lines are spaced by $5\,\mathrm{K}$) and (g-i) concentrations profiles (the isoconcentration lines are spaced by 0.04) in the xy-plane ($z = 0$). As the distance from the center of the trap increases, the drift due to the optical forces (red arrows) increases and the diffusiophoretic drift (green arrows) decreases. The presence of small asymmetries in the temperature and demixing profile around the particle make it rotate around the optical axis; the corresponding tangential force (gray arrow) is maximized at the equilibrium configuration where the optical-force-induced drift balances the diffusiophoretic drift. (a), (b), and (c) correspond to Fig. 1(a), 1(c), and 1(b) respectively. See also the corresponding supplementary Video 3.
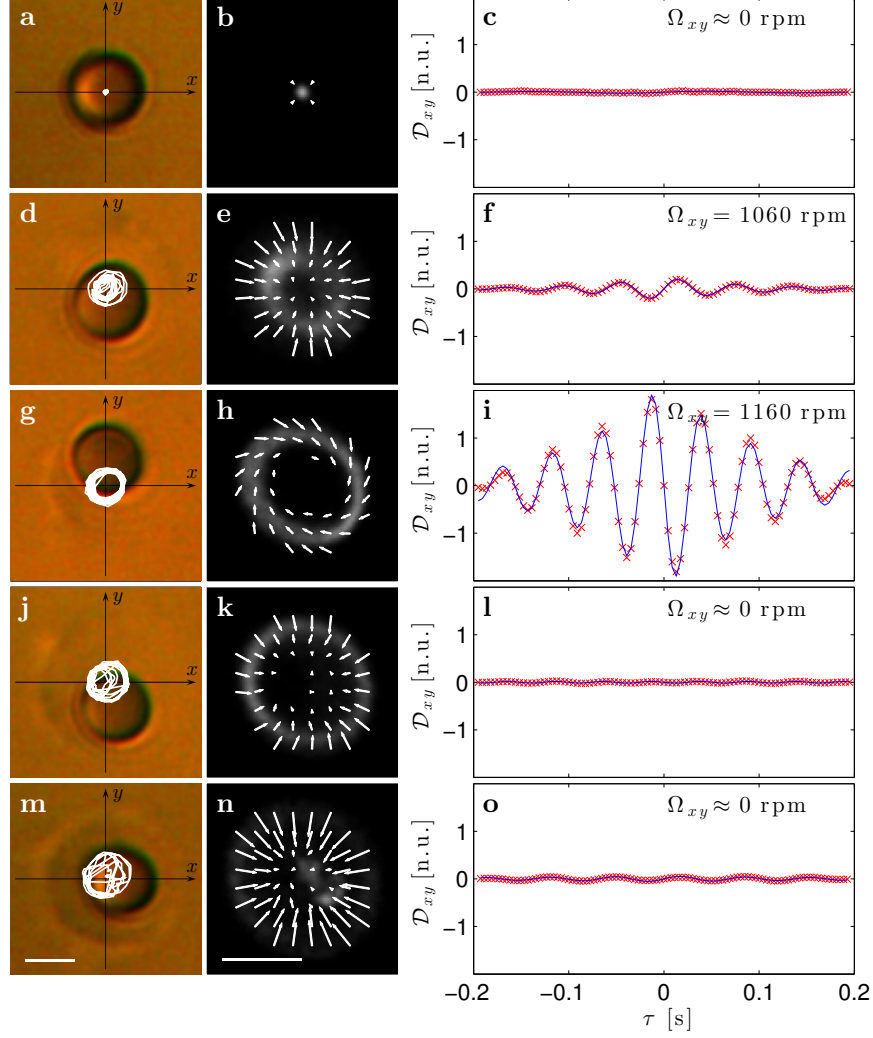
FIG. S4: Engine performance as a function of ambient temperature for a particle with $R = 1.24\,\mu$m. The laser power at the optical trap is fixed at $P = 2.7\,$mW, while the ambient temperature of the sample is (a-c) $T_0 = 20$, (d-f) 24, (g-i) 26, (j-l) 27, and (m-o) 28°C. (a,d,g,j,m) Bright-field images of the particle with $0.6\,$s trajectories represented by white solid lines. (b,e,h,k,n) Velocity drift fields (white arrows) and particle position probability distributions (background color, brighter colors represent higher probability density). (c,f,i,l,o) Experimental (red symbols) and fitted (blue solid lines) differential cross-correlation functions $\mathcal{D}_{xy}$ in the xy-plane, from which the rotation rate of the particle Ω_{xy} can be obtained as fit parameter (reported in the right column). The white bars in (m) and (n) correspond to $1\,\mu$m. (g-i) are the same data as Fig. 2j-l. See also supplementary Video 2.
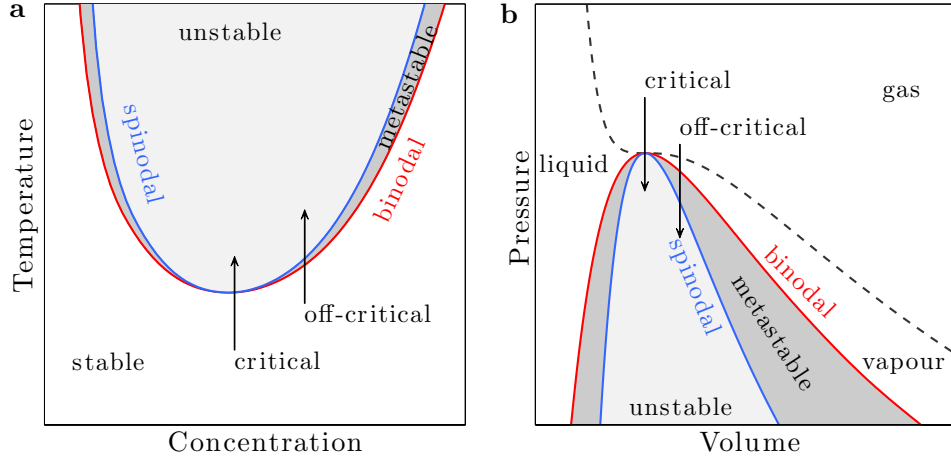
FIG. S5: Schematic phase diagram of a mixture showing the spinodal and binodal lines. The distance between the two lines is related to the latent energy required for the phase separation to occur. Only at the critical point the two lines coincide and, therefore, there is no latent energy and hysteresis. (a) Phase diagram depending on temperature and concentration corresponding to our realization of the critical engine. (b) Phase diagram depending on pressure and volume as an alternative system in which the proposed critical engine can operate (note the upper critical point).
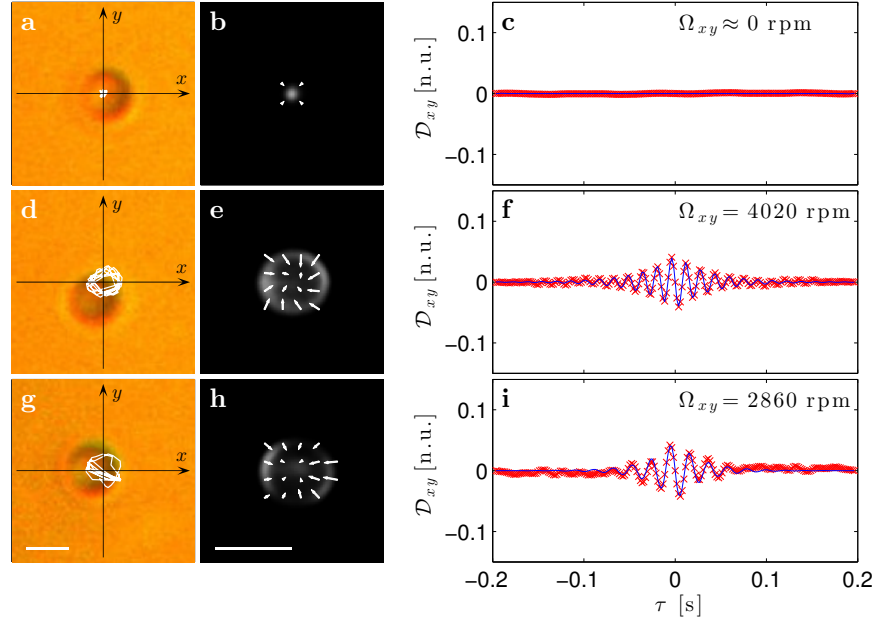
FIG. S6: Engine performance as a function of laser power for a particle with $R = 0.49\,\mu$m. The ambient temperature of the sample is fixed at $T_0 = 21°$C, while the laser power at the optical trap is (a-c) $P = 0.6$, (d-f) 1.5, and (g-i) 2.7 mW. (a,d,g) Bright-field images of the particle with 0.1 s trajectories represented by white solid lines. (b,e,h) Velocity drift fields (white arrows) and particle position probability distributions (background color, brighter colors represent higher probability density). (c,f,i) Experimental (red symbols) and fitted (blue solid lines) differential cross-correlation functions $\mathcal{D}_{xy}$ in the xy-plane, from which the rotation rate of the particle Ω_{xy} can be obtained as fit parameter (reported in the right column). The white bars in (g) and (h) correspond to 1 μm.
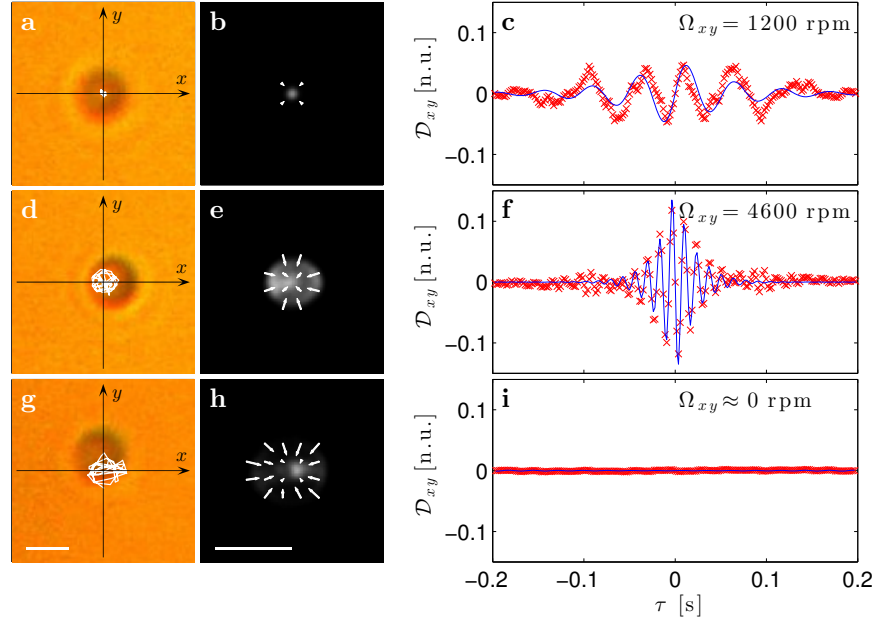
FIG. S7: Engine performance as a function of ambient temperature for a particle with $R = 0.49\,\mu m$. The laser power at the optical trap is fixed at $P = 1.5\,mW$, while the ambient temperature of the sample is (a-c) $T_0 = 19.5$, (d-f) 23, and (g-i) 27°C. (a,d,g) Bright-field images of the particle with $0.1\,s$ trajectories represented by white solid lines. (b,e,h) Velocity drift fields (white arrows) and particle position probability distributions (background color, brighter colors represent higher probability density). (c,f,i) Experimental (red symbols) and fitted (blue solid lines) differential cross-correlation functions $\mathcal{D}_{xy}$ in the xy-plane, from which the rotation rate of the particle Ω_{xy} can be obtained as fit parameter (reported in the right column). The white bars in (g) and (h) correspond to $1\,\mu m$.

[1] A. Würger. Self-diffusiophoresis of Janus particles in near-critical mixtures. *Phys. Rev. Lett.*, 115:188304, 2015.

[2] G. Volpe and D. Petrov. Torque detection using Brownian fluctuations. *Phys. Rev. Lett.*, 97:210603, 2006.

[3] G. Volpe, G. Volpe, and D. Petrov. Brownian motion in a nonhomogeneous force field and photonic force microscope. *Phys. Rev. E*, 76:061118, 2007.

[4] P. H. Jones, O. M. Maragò, and G. Volpe. *Optical tweezers: Principles and applications.* Cambridge University Press, Cambridge, UK, 2015.

[5] G. Pesce, G. Volpe, A. Imparato, G. Rusciano, and A. Sasso. Influence of rotational force fields on the determination of the work done on a driven brownian particle. *J. Opt.*, 13(4):044006, 2011.

[6] C. A. Grattoni, R. A. Dawe, C. Y. Seah, and J. D. Gray. Lower critical solution coexistence curve and physical properties (density, viscosity, surface tensio, and interfacial tension) of 2,6-lutidine + water. *J. Chem. Eng. Data*, 38:516–519, 1993.

[7] E. J. G. Peterman, F. Gittes, and C. F. Schmidt. Laser-induced heating in optical traps. *Biophys. J.*, 84(2):1308–1316, 2003.

[8] S. Samin and R. van Roij. Self-propulsion mechanism of active Janus particles in near-critical binary mixtures. *Phys. Rev. Lett.*, 115:188305, 2015.